AEROHEATING ANALYSIS
FOR PLANETARY RE-ENTRY VEHICLES

Alvin Murray
ITT Industries
Missile Defense Group
6767 Old Madison Pike, Ste 310
Huntsville, AL 35806
256-971-1506
al.murray@itt.com

ABSTRACT

This paper demonstrates the use of the Aeroheating and Thermal Analysis Code (ATAC) for planetary re-entry environments. This tool was developed under an Army SBIR contract with the objective to integrate the Maneuvering Aerotherm Shape Change Code (MASCC) with the Charring Material Thermal Response and Ablation Code (CMA) and provide a means of generating finite element thermal boundary conditions for missile design. ATAC represents the state-of-the-art in efficient aerothermal heating analysis. The code uses the axisymmetric analogy and solves the integral momentum and energy boundary layer equations along streamlines around the body providing a means of obtaining 3-dimensional transient aerothermal boundary conditions. Coupling of CMA with MASCC provides detailed 1D in-depth transient thermal solutions at each node point on the body for a single analysis run. The surface temperature and ablation mass flux are explicitly coupled with the flowfield solution providing realistic transient hot wall boundary conditions for more detailed thermostructural finite element analysis.

The capabilities of ATAC are demonstrated with three re-entry studies. The first study compares the high altitude aerodynamics predictions with Direct Simulation Monte Carlo calculations and with data from the Viking program. The second study compares with aeroheating data on large-angle spherically blunted conical bodies. The third study will be comparisons with thermocouple data taken from the Shuttle re-entry flights.

INTRODUCTION

The purpose of this paper is to describe a process for predicting the aeroheating and thermal response of blunt re-entry configurations in high-speed flows. These predictions are the required inputs to determine the survivability of a conceptual design and provide a needed evaluation of a design without having to build multiple prototypes for testing and evaluation. The flight regime of most interest is that of supersonic-hypersonic continuum flow in which the heat flux is sufficient to cause ablation at some locations on the surface.

In the past, flowfield solutions were generated during a specified flight using the Maneuvering Aerotherm Shape Change Code, MASCC.[1] At specified times, these boundary conditions were

applied to a Charring Material Thermal Response and Ablation Program, CMA[2] finite difference model to obtain the transient thermal response at each of the surface nodes. The effects of changes in the surface temperature, ablation and pyrolysis mass fluxes, and the shape of the vehicle were not included in the analysis unless the user modified the MASCC input and re-ran the flowfield solutions. This would require a large number of CMA solutions to model the surface response and would be very labor intensive. The Aeroheating and Thermal Analysis Code (ATAC)[3] combines MASCC and CMA to provide an efficient and cost effective procedure for incorporating these effects into a thermal analysis. The methodologies used in ATAC are briefly described in the following sections.

FLOWFIELD ANALYSIS

ATAC includes a completely general three-dimensional flowfield solver that uses semiempirical procedures to determine the flowfield on missile configurations. The code offers significant efficiency advantages for design purposes over computational fluid dynamics (CFD) codes that solve the full Navier Stokes equations. The hundreds of flowfield and boundary layer solutions that are required to model a complete trajectory, requires only a few minutes with ATAC. CFD techniques, on the other hand, would require very fine grids to resolve boundary layers and this would result in extremely long run times to model the many different flight conditions that must be considered. Ideally, CFD techniques can be used in concert with ATAC to refine specific areas of complex flowfield phenomena and shock interactions when necessary.

ATAC can be used to calculate the surface heat flux based on the velocity, altitude, and angle of attack throughout the flight of interest. The basic inputs needed are the body configuration, angle of attack, and the freestream conditions. The geometry is described in ATAC with a system of Coon's bi-cubic patches[4]. These patches allow general geometries and facilitate the calculation of the surface coordinates and gradients at points intermediate to the nodal system. In ATAC, the axisymmetric analogy is used for the prediction of the flowfield. Using this approximation, the axisymmetric equations for the inviscid and viscous flow are integrated along various streamlines. An effective radius, or metric coefficient replaces the radius in the axisymmetric equations.

INVISCID STEAMLINE TRACING

The flowfield solution is performed along each of the calculated inviscid streamlines. The method used in ATAC to calculate these streamlines is known as the Newtonian approximation or the method of steepest descent. The Newtonian flow model assumes that a stream of particles impinging on a surface retains its tangential component of momentum. Therefore, an instantaneous velocity direction at each point on the body is defined by

$$\vec{v} = \hat{n} \times \left(\vec{V}_\infty \times \hat{n} \right)$$

By converting $\vec{v}$ to a unit tangent vector, the derivatives of the surface parameters with respect to the streamline arc length may be determined in the following manner. If $\vec{r}$ is the position

vector of some point on the body, the parametric representation of the body geometry provides $\vec{r}$ as a function of the surface parameters w and u. The unit tangent vector at the point may then be written

$$\hat{t} = \frac{d\vec{r}}{ds} = \frac{\partial \vec{r}}{\partial w}\frac{dw}{ds} + \frac{\partial \vec{r}}{\partial u}\frac{du}{ds} \tag{1}$$

Any two of the three Equations (1) may be solved for dw/ds and du/ds, the slopes in each of the two surface coordinate directions. This algorithm can be started at any point on the body and integrated either upstream or downstream.

One of the most difficult problems in coupling a shape change procedure with a three-dimensional flowfield analysis is an accurate prediction of the environment at each shape change point. With a streamline tracing procedure, such as the one used in ATAC, this problem is even more complicated because the location of the streamlines is difficult to control as the nosetip ablates. The ATAC procedure begins at the back of the vehicle and traces a streamline forward to the stagnation point. This assures a reasonable distribution at the end of the vehicle and eliminates the effects of the ablated nosetip on the streamlines. To provide adequate coverage at the nosetip, a streamline addition procedure is used which establishes additional streamlines on the vehicle.

SURFACE PRESSURE

The ATAC code has three options for computing surface pressure distributions on the windward streamlines: (1) the Dahm-Love pressure correlations used in ASCC,[5] (2) a Newtonian pressure model with modifications for Mach number effects,[6] or (3) a modified Newtonian pressure model for sharp nosed vehicles.[7] Pressures on the leeward or shadow regions are calculated using: (1) the Newtonian approximation ($C_p = 0$), (2) hypersonic small disturbance theory,[8] or (3) a pressure correlation for separated flows.[8] In general, the Dahm-Love correlations are used for blunt, short, sphere-cone geometries. The modified Newtonian model is used for ogives and other sharp-nosed configurations.

SHOCK SHAPE

A thin-shock layer integral technique is used in ATAC to compute the shock shape. The global continuity and axial momentum equations are cast in integral form. The global continuity equation is given by:

$$\rho_\infty u_\infty \pi R^2 = 2\pi \int_0^{\delta_s} \rho u r\, dy$$

and the global axial momentum

$$\left(p_\infty + \rho_\infty u_\infty^2\right)\pi R^2 = \int_0^{\delta_s} \rho u(u\cos\theta + v\sin\theta)\,2\pi r\,dy + \int_0^{s}\left(p_w \sin\theta\right)2\pi r_w\,ds + \int_0^{\delta_t}\left(p\cos\theta\right)2\pi r\,dy$$

The integrands are assumed to vary linearly between the body surface and shock. The flow properties behind the shock are related to freestream conditions via oblique shock relations and

the equation of state. With the known pressure distribution along the wall, together with the assumed integrand functional form and behind-the-shock properties, the continuity and axial momentum equations are solved for shock standoff distance and shock angle. The standoff distance and angle are related by geometry, which serves as a boundary condition, rendering an elliptic system of equations, which must be iterated for the standoff distance along the body. Decoupling the geometry constraint from the system of equations eliminates the iteration. This approach results in an initial value problem. The control volume for the thin shock layer solution is shown in Fig. 1.
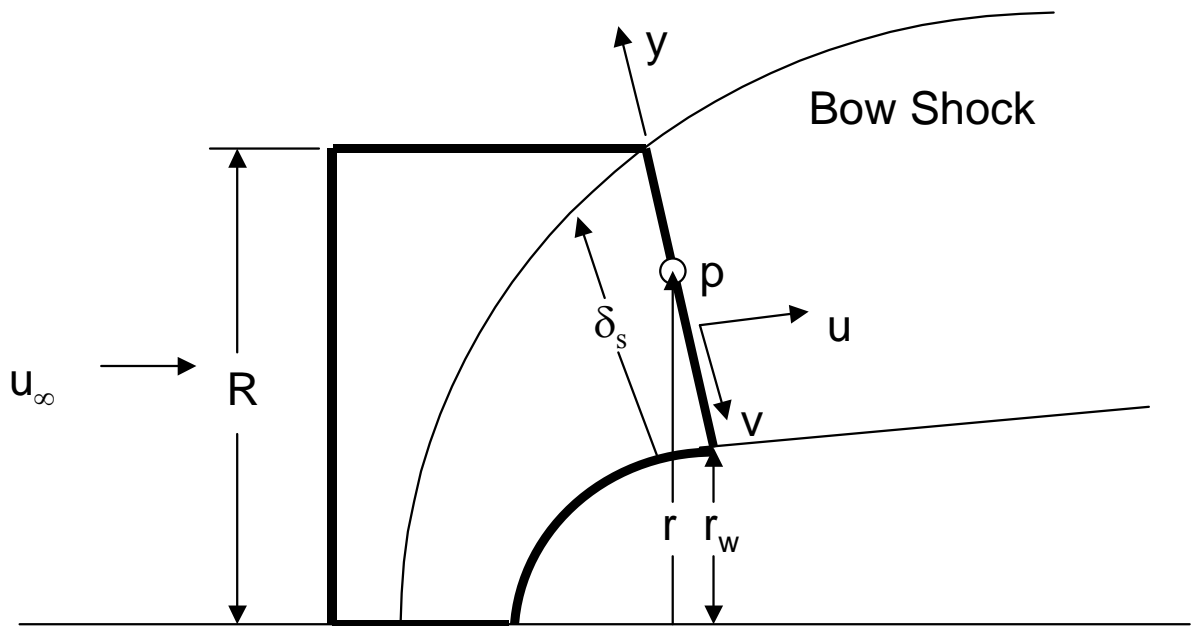
Figure 1: Control Volume for the Shock Shape Solution

BOUNDARY LAYER TECHNIQUE

The boundary layer scheme employed in ATAC is known as the Momentum /Energy Integral Technique (MEIT). MEIT has also been used in the ABRES Shape Change Code, ASCC[5] and Three Dimensional Momentum / Energy Integral Technique (3DMEIT) codes and is essentially the same in all of these procedures. The current modifications in ATAC incorporate the latest developments in MEIT and the procedure should be the same as that used in ASCC86 except for the metric coefficient and differences in the body slopes due to the different geometry specification. In MEIT, the baseline relationships are those for C_f and C_h as functions of

Re_θ and Re_ϕ on an incompressible flat plate. The effects of other phenomena are included as multiplicative factors, called influence coefficients, which are applied to the baseline expressions. A theoretical justification for this approach is the work of Kutateladze and Leont'ev[9, 10] who show that the asymptotic behavior of the shear and heat transfer for compressible boundary layer flow over a flat plate in the limit of infinite Reynolds number differ

from the corresponding incompressible case by a factor they call Ψ, which is exactly the influence coefficient used in MEIT

The following three basic equations are solved simultaneously in the MEIT procedure: Integral momentum equation:

$$\frac{1}{r\rho_e u_e^2}\frac{d}{ds}(r\rho_e u_e^2\Theta) = \frac{C_f}{2} + \frac{(\rho v)_w u_{i,w}}{\rho_e u_e^2} + \frac{H\Theta}{\rho_e u_e^2}\frac{dp}{ds} \tag{2}$$

Integral energy equation:

$$\frac{1}{r\rho_e u_e(h_{t,e}-h_w)}\frac{d}{ds}\left(r\rho_e u_e(h_{t,e}-h_w)\,\Phi\right) = C_h\frac{h_r-h_w}{h_{t,e}-h_w} + \frac{(\rho v)_w(h_{t,i,w}-h_w)}{\rho_e u_e(h_{t,e}-h_w)} \tag{3}$$

Entrainment relation:

$$\rho_\infty u_\infty \bar{y}^2 = 2rF\mu_e\,\mathrm{Re}_\theta - 2\int_0^\infty r(\rho v)_w\,ds \tag{4}$$

The momentum equation solution dictates the skin friction and momentum thickness upon which the following phenomena are based: 1) transition onset and location, 2) transitional intermittency, 3) surface roughness effects, 4) turbulent boundary layer shape factors, and 5) entrainment rate. The energy equation solution dictates the convective heat transfer subject to these five parameters.

The entrainment relation, Eq. (4), provides a means of determining the boundary layer edge properties that are essential boundary conditions for the solution of Eqs. (2) and (3). The boundary layer edge thermodynamic state is determined by lookup on pressure and entropy in a real-gas Mollier table. Pressure is known from the inviscid flow solution, and entropy is calculated from consideration of the bow shock shape and boundary layer mass entrainment. Figure 2 illustrates the method and basis for the mass balance that leads to Eq. (4).

Basic Boundary Layer Laws

The friction factor and Stanton number are represented by $C_{x,y,0}$ where the subscript 0 denotes the basic laws, x = f for friction factor and x = h for Stanton number. The state of the boundary layer is shown by the subscript y. Subscript ℓ is used for laminar flow and t for turbulent flow.
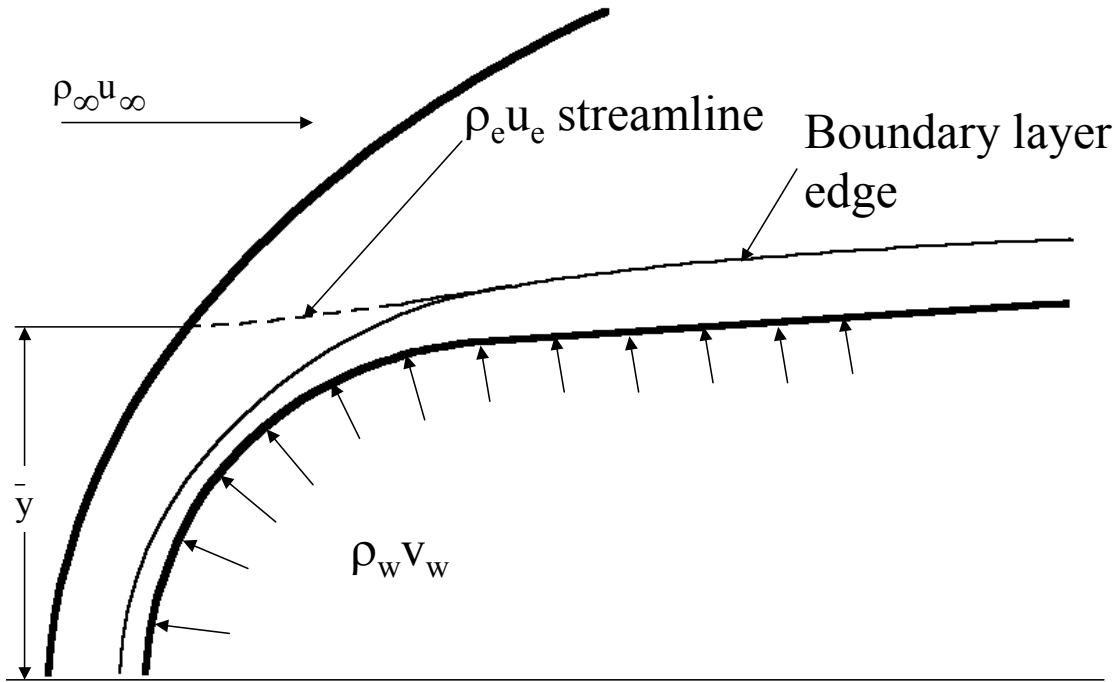
Figure 2: Sketch of the Boundary Layer Mass Entrainment Method

The basic laws for the friction and Stanton number are:

Laminar Flow:

$$\frac{C_{f,\ell,0}}{2} = \frac{0.220}{Re_\Theta}$$

$$C_{h,\ell,0} = \frac{0.220}{Pr^{4/3} Re_\Phi}$$

Turbulent Flow:

$$\frac{C_{f,t,0}}{2} = \frac{0.245}{Re_\Theta} + \frac{0.010742 Re_\Theta}{100 + Re_\Theta} \left(\log_{10} Re_\Theta\right)^{-1.5262}$$

$$C_{h,t,0} = \frac{0.22}{Pr^{4/3} Re_\Phi} + \frac{a\, Re_\Phi}{\left(100 + Re_\Phi\right)} \left(\log_{10} Re_\Phi\right)^{-b}$$

For Pr ≥ 0.6,
$$a = 0.0993e^{(0.0648\,\text{Pr})}\big/(1.0 + 9.6\,\text{Pr})$$
$$b = 1.954e^{(0.273\,\text{Pr})}\big/(1.0 + 0.71\,\text{Pr})$$

and for Pr < 0.6,
$$a = 0.1256e^{(0.2435\,\text{Pr})}\big/(1.0 + 14.2\,\text{Pr})$$
$$b = 2.217e^{(0.6313\,\text{Pr})}\big/(1.0 + 1.677\,\text{Pr})$$

Transitional and Non Ideal Effects

For natural transition, the dependence of the parameters $C_f/2$, C_h, H, F and R (the recovery factor) on the boundary layer state is established via the transitional intermittency factor. This factor is zero in laminar flow, unity in turbulent flow and between 0 and 1 for transitional flow. The transitional intermittency that is employed in ATAC is based on the work of Persh, according to the interpretation of Dahm[5].

Non-ideal effects are modeled through the use of influence coefficients. These coefficients are factors that are derived by comparing the convective transfer with the ideal flat-plate result for the same boundary layer state. These factors are generally derived for only one non-ideal mechanism at a time. The MEIT procedure assumes that the Stanton number, C_h, and the friction factor, $C_f/2$, can be written as:

$$C_{x,y} = C_{x,y,0} \prod^{z} I_{x,y,z} \text{ for } x = h, f \text{ and } y = \ell, t$$

where $C_{x,y,0}$ refers to the basic law for incompressible flow along an impervious, isothermal flat plate, x indicates heat or momentum transfer, y indicates laminar or turbulent flow, and z indicates the non-ideal effect being considered. Current effects modeled in ATAC include acceleration caused by finite pressure gradients, real gas and Mach number effects, surface roughness, and mass transfer. A complete description of these models is given by Murray.[3]

High Altitude Flowfield Modeling and Bridging Functions

At very high altitudes, the molecular mean free path λ may be large compared to a characteristic body dimension ℓ. This means that molecules, which impinge upon a body and then are re-emitted, will not collide with other molecules until very far away from the body. The dimensionless parameter, which describes the degree of rarefaction of the gas, is the Knudsen number, λ/ℓ. It is often convenient to divide various flow regimes in terms of the Knudsen number. When the mean free path is large compared to the characteristic body dimension (Kn > 10), the flow is termed free molecular. If the mean free path is on the same order of magnitude as the characteristic dimension of the flowfield ($0.1 < \text{Kn} < 10$), then the flow regime is called transitional. Whenever the gas layer adjacent to a surface slips ($0.01 < \text{Kn} < 0.1$), flow is in the temperature jump (or slip) regime. For very small Knudsen numbers (Kn < 0.01), the flow is called continuum, i.e., the Navier-Stokes equations and the Fourier heat conduction law are valid.

High-altitude models for heating, pressure, and shear stress model have been incorporated into ATAC. In these models, the flow is divided into three regimes: free molecular, transitional, and continuum. Transitional heating is computed by appropriately combining the free molecular and continuum values using a bridging function. This method implicitly requires that the free molecular and continuum values behave in a regular manner as Kn → 0 and Kn → ∞, respectively.

The heating and shear stress in a free molecular environment are well understood, and problems in this flow regime can be solved in closed analytical form. In the free molecular flow regime, the flux of energy to a body is given by Schaaf and Chambre.[11]

$$\dot{q} = \alpha \rho R T_\infty \sqrt{\frac{RT_\infty}{2\pi}} \left[\left(s^2 + \frac{\gamma}{\gamma-1} - \frac{\gamma+1}{2(\gamma-1)} \frac{T_w}{T_\infty} \right) \left(e^{-(s\sin\theta)^2} + \sqrt{\pi}(s\sin\theta)[1 + \mathrm{erf}(s\sin\theta)] \right) - \frac{1}{2} e^{-(s\sin\theta)^2} \right]$$

where α is the thermal accommodation coefficient, s is the molecular speed ratio defined as $V_\infty / \sqrt{2RT_\infty}$, and θ is the angle between the surface and the flow direction.

The shear stress in the free molecular regime is

$$\tau = \frac{\sigma \rho V^2 \cos\theta}{2s\sqrt{\pi}} \left[e^{-(s\sin\theta)^2} + \sqrt{\pi}(s\sin\theta)[1 + \mathrm{erf}(s\sin\theta)] \right]$$

where σ is the tangential surface reflection coefficient.

The surface pressure on a body in the free molecular regime is

$$p = \frac{\rho V^2}{2s^2} \left[\left(\frac{2-\sigma'}{\sqrt{\pi}} s\sin\theta + \frac{\sigma'}{2} \sqrt{\frac{T_w}{T_\infty}} \right) e^{-(s\sin\theta)^2} + \left[(2-\sigma') \left(s^2 \sin^2\theta + \frac{1}{2} \right) + \frac{\sigma'}{2} \sqrt{\frac{\pi T_w}{T_\infty}} (s\sin\theta) \right] [1 + \mathrm{erf}(s\sin\theta)] \right]$$

where σ' is the normal surface reflection coefficient.

The above relations require knowledge of the surface temperature. This information is generally not known a priori. However, the term containing the surface temperature ratio becomes negligible as s → ∞. Thus, if one is mainly interested in hypersonic flows, a value of the surface temperature ratio can be assumed without being in large error. For our implementation, the wall temperature is taken from the previous time step, when surface energy balance calculations are performed. For cases when no surface energy balance is performed, the constant wall temperature input by the user is used.

Prediction of the physics in the transitional regime presents a formidable challenge. Several computational techniques currently exist, but each method is at least as hard to solve as the Navier-Stokes equations, e.g., model equations and moment methods[12], or requires an extremely large amount of computer time, e.g., Monte Carlo simulations.[13] The approach taken here to compute transitional properties is very simple and consists of combining the free molecular and continuum value using an appropriate bridging relation. Two bridging functions are used in ATAC based on the work of Matting.[14]

For transitional pressure the relation is

$$p = p_{cont}\left(1 + \frac{p_{fm} - p_{cont}}{p_{cont}}e^{(-7.3246 \times 10^6 R_n \rho_\infty)}\right)$$

The bridging function for heating and shear stress is

$$x = x_{cont}\left(1 - e^{-x_{fm}/x_{cont}}\right), x = f, h$$

CMA TRANSIENT THERMAL ENVIRONMENT

CMA uses an implicit, finite-difference procedure for computing the one-dimensional transient transport of thermal energy in a material that can ablate from a front surface and decompose in-depth. Figure 3 illustrates the general physical problem treated by CMA. As the material is heated, one or more components of the original composite material pyrolyzes and yields a pyrolysis gas and a porous residue. The pyrolysis gas percolates away from the pyrolysis zone. The residue, for many materials of interest, is a carbonaceous char possibly reinforced with refractory fibers or cloth.
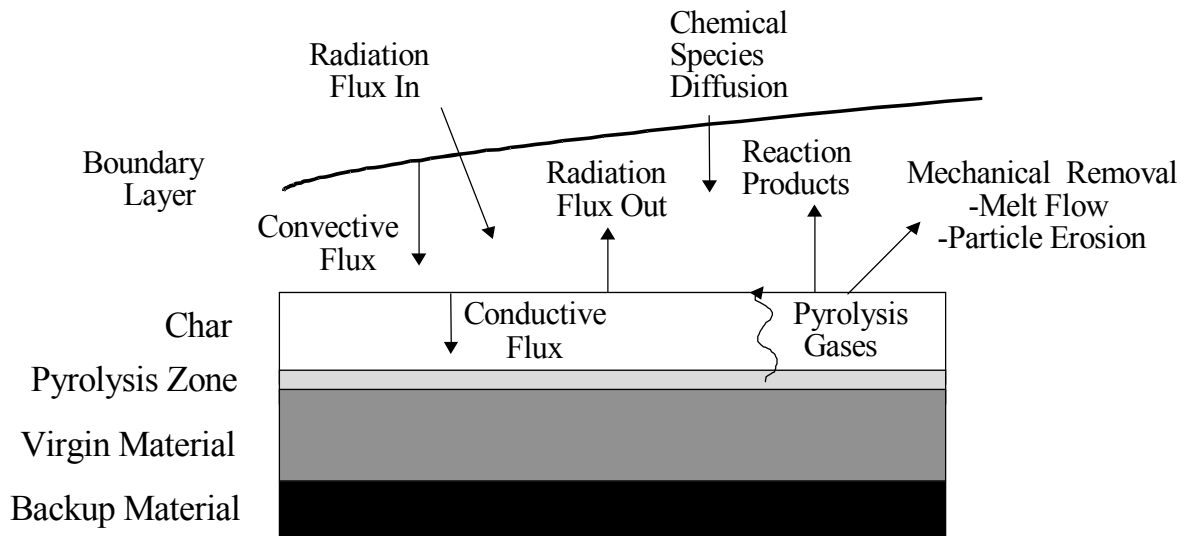
Figure 3: Schematic of the general surface energy balance

The in-depth solution procedure is basically a transient heat conduction calculation coupled to a pyrolysis rate calculation and to boundary conditions from the flowfield solution. The coupling with the boundary conditions is provided through a surface energy balance solution.

RESULTS

Calculations have been conducted for three test cases to demonstrate the capabilities of the code. These test cases are for very blunt reentry vehicles such as the Pascal Entry, Descent and Landing (EDL) Module and the Mars Smart Lander (MSL). The first case compares the ATAC aerodynamic predictions to Direct Simulation Monte Carlo (DSMC) calculations and with flight data from the Viking program. The second case is a comparison with data from test on the Mars Smart Lander and with data measured by Stewart on large-cone blunted cones. The third case is comparison with flight data from STS-96.

VIKING AERODYNAMIC PREDICTIONS

The transition between free molecular and continuum flow during the high altitude portion of a re-entry flight was studied by Wilmoth, Blachard and Moss.[15] Calculations were done with Monte Carlo techniques and bridging correlations and comparisons were made with data from the Viking Martian entry. Calculations for the Pascal EDL Module were done to check the use of the Matting[14] bridging functions in ATAC. Figure 4 compares the predicted transition of the axial force coefficient, c_a with the DSMC calculations for several Martian entry vehicles. The magnitude of the axial force coefficient is different from these other vehicles due to differences in the geometries. However, the Matting bridging correlation also predicts a significantly slower transition from free-molecular flow. Since the pressure is the dominate factor of these blunt body configurations, the bridging function on the pressure was replaced with the relation given by Ivanov.[16]

$$p = p_{cont}(1 - P_b) + p_{fm}P_b$$

where

$$P_b = \frac{1}{2}\left(1 + erf\left\{\frac{\sqrt{\pi}}{\Delta Kn}\log\left[\frac{Kn_{\infty}}{Kn_m}\right]\right\}\right)$$

Kn_m is the Knudsen number at the center of the transitional regime where $P_b = $ ½ and ΔKn is the logarithmic width of the transitional regime. This function was used in Reference 15 and shown to provide good correlation with the calculations and flight data. In ATAC, these correlations are used as local bridging functions as opposed to the global application used by Wilmoth.[15] A local function is applied to the surface pressure and wall shear which are then integrated to determine the aerodynamic coefficients. For global applications, the bridging functions are applied to the aerodynamic coefficients directly. Predictions using the "erf" model are also shown in Figure 4 and the agreement with the shape of the transition curve is much better. Figure 5 compares the ATAC calculations of C_n/C_a with the DSMC calculations and the Viking flight data. The prediction using the erf bridging function is in good agreement with the other calculations and the flight data.
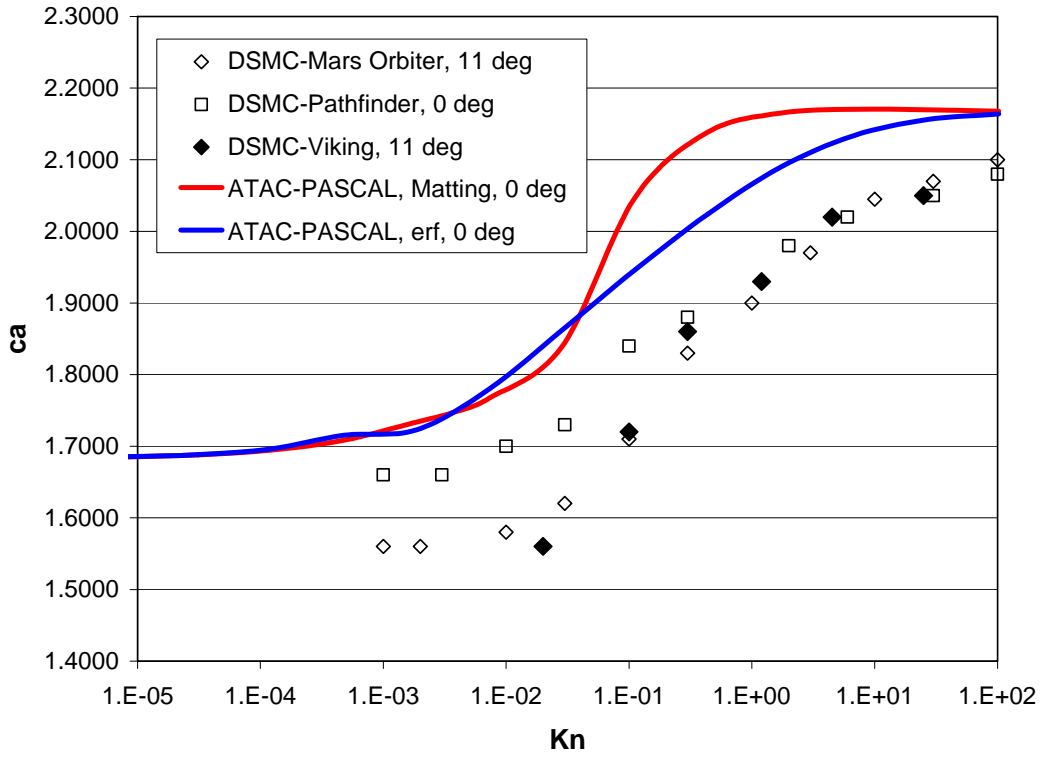
Figure 4: Comparison of axial force coefficient predictions for various entry configurations
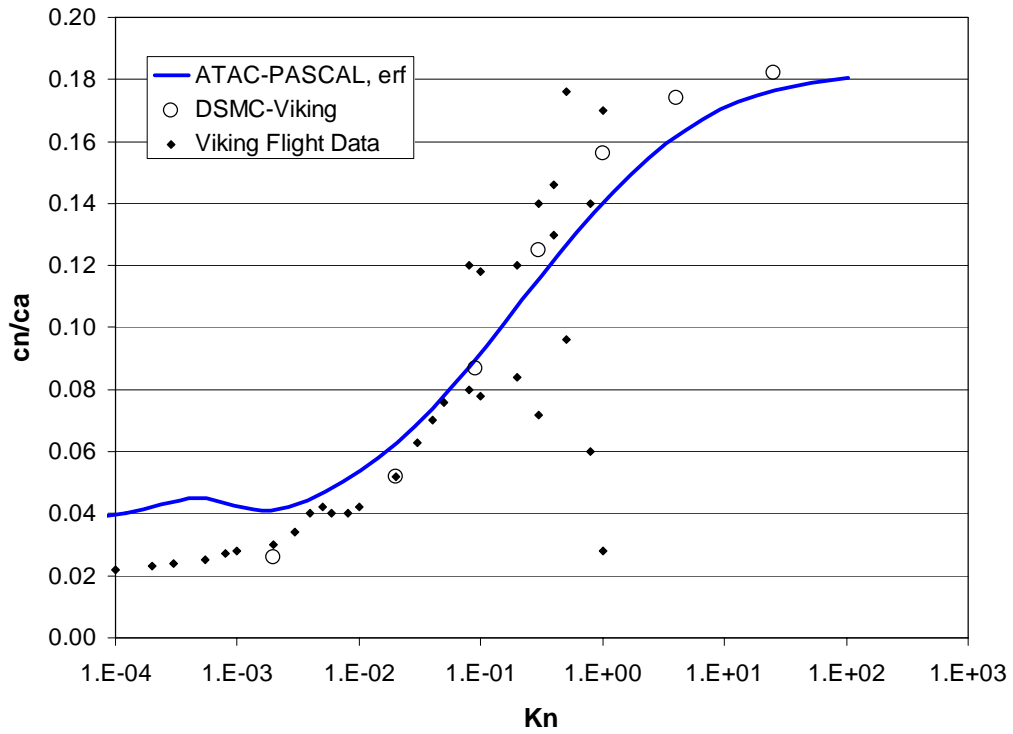
Figure 5: Comparison of predicted aerodynamics with Viking flight data

MARS SMART LANDER

The Mars Smart Lander is intended to enter the Martian atmosphere and land with an uncertainty of less that 10 km. One of the design issues for this vehicle is the transition of the boundary layer to turbulent flow. A study was conducted by Hollis and Liechty[17] to formulate transition criteria for the Martian entry. Global surface heating distributions were obtained using phosphor thermography and comparisons were made with Navier-Stokes calculations using LAURA. The heating data were presented in a non-dimensional form, h/h_{FR} where h_{FR} is the reference heat-transfer coefficient from Fay Riddell theory using the nose radius of the model and a 300K surface temperature. Calculations were done for the $Re_\infty/m=1.4x10^7$ condition and the results are shown in Figure 6. ATAC grossly overpredicted the heating on the nosetip but was in good agreement on the cone for r/R greater than 0.5. The ATAC solution is predicting the Fay-Riddell value for the nosetip since the code does not predict the pressure accurately on the large-angle conical configurations. Previous results on the Apollo capsule showed excellent agreement with wind tunnel and flight data,[18] but the Apollo heat shield consists of a uniform radius instead of the large-angle blunted cone used in the MSL configuration.
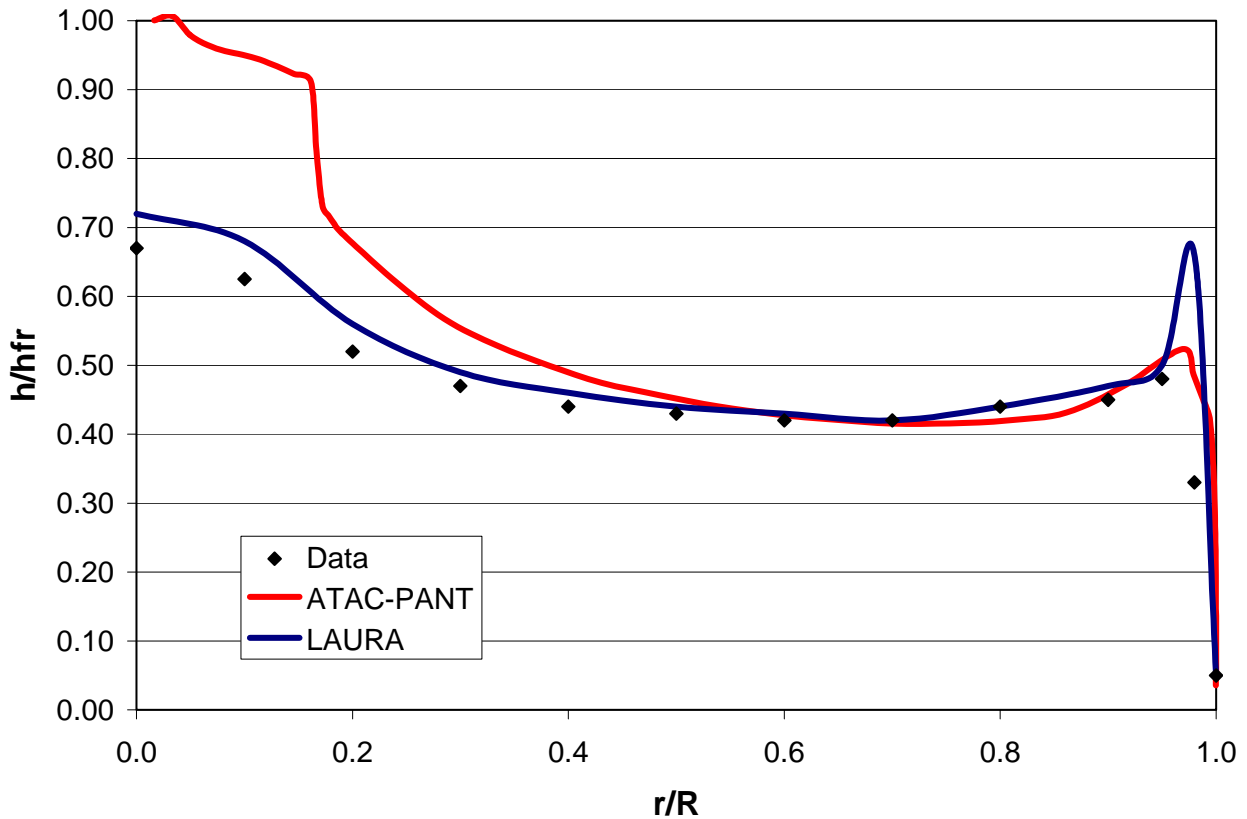
Figure 6: Comparison with MSL data at α=0

The Dahm-Love pressure correlation developed under the PANT program allowed for blunt geometries and included a bridging between the Newtonian and flat faced cylinder pressure distributions. The correlation in the subsonic region is given by:

12

$$\bar{p}=\bar{p}_{mn}-(1-\bar{p}_{fd})\left[\frac{\bar{p}_{mn}-\bar{p}^*}{1-\bar{p}^*}\right]+\left(1-\frac{R_n}{R_{max}}\right)\left\{\left(1-\frac{s}{s^*}\right)(1-\bar{p}_{\infty})\cos^2\theta+\frac{1}{2}\frac{s}{s^*}\left[\bar{p}_{fd}-1+\frac{s}{s^*}(1-\bar{p}_{\infty})\cos^2\theta+\left(1-\bar{p}_{fd}\right)\left(\frac{\bar{p}_{mn}-\bar{p}^*}{1-\bar{p}^*}\right)\right]\right\}$$

where,

$\bar{p}$ = p/p_0

p_0 = stagnation pressure

$\bar{p}_\infty$ = freestream pressure ratio

$\bar{p}_{mn}$ = modified Newtonian pressure

$\bar{p}_{fd}$ = pressure on a flat-faced cylinder

R_n = stagnation point radius of curvature

R_{max} = max (R_n, R^*)

R^* = distance from sonic point to body axis, measured normal to the surface at the sonic point

To determine why this correlation was failing to predict the pressure on these blunt configurations, comparisons were made with data from Stewart and Marvin[19] and Stewart and Inouye.[20] Calculations were performed with the Newtonian and the PANT pressure models and comparisons were made with the heat-flux measurement in Reference 19. Figure 7 compares the heating distributions on a 50 degree cone while Figure 8 presents the results for the 70 degree cone. At 50 degrees, the PANT pressure model predicts a much lower heating rate at the stagnation point than does the Newtonian model. At 70 degrees, the two pressure models predict nearly the same values for the stagnation heating. Even at 60 degrees, the PANT and Newtonian models were in reasonable agreement but were much higher than the experimental data. At 60 degrees and above, the PANT correlations were reduced to the Newtonian values instead of using the bridging between the Newtonian and flat-faced cylinder. Figures 8 and 9 show the pressure distributions on the 50 and 70 conical bodies and verify that at the larger cone angles, the PANT model produces the same velocity gradient at the nosetip as does the Newtonian model. The difficulty was traced to the calculation of the effective nose radius, R_n. In ATAC, this radius is calculated from the shape of the vehicle at the nose. The logic integrates the gradients of the surface out to the first point where the body angle is less than 50.5 degrees and uses these integrals to calculate the effective stagnation point radius. For the 50 degree configuration, the calculated R_n was very close to the nose radius but for angles greater that 50, the calculated R_n was much larger. The calculated value was larger than the R^* calculated from the sonic point logic so the value of R_{max} was equal to R_n. This removed the last term in the pressure correlation and the PANT model predicted a distribution very close to the Newtonian value.

A modification was made in the nosetip logic that limited the integration of the surface to the actual nosetip of the body. The predicted values of R_n were very close to the nose radius for all cone angles and there was a substantial improvement in the pressure gradient at the stagnation
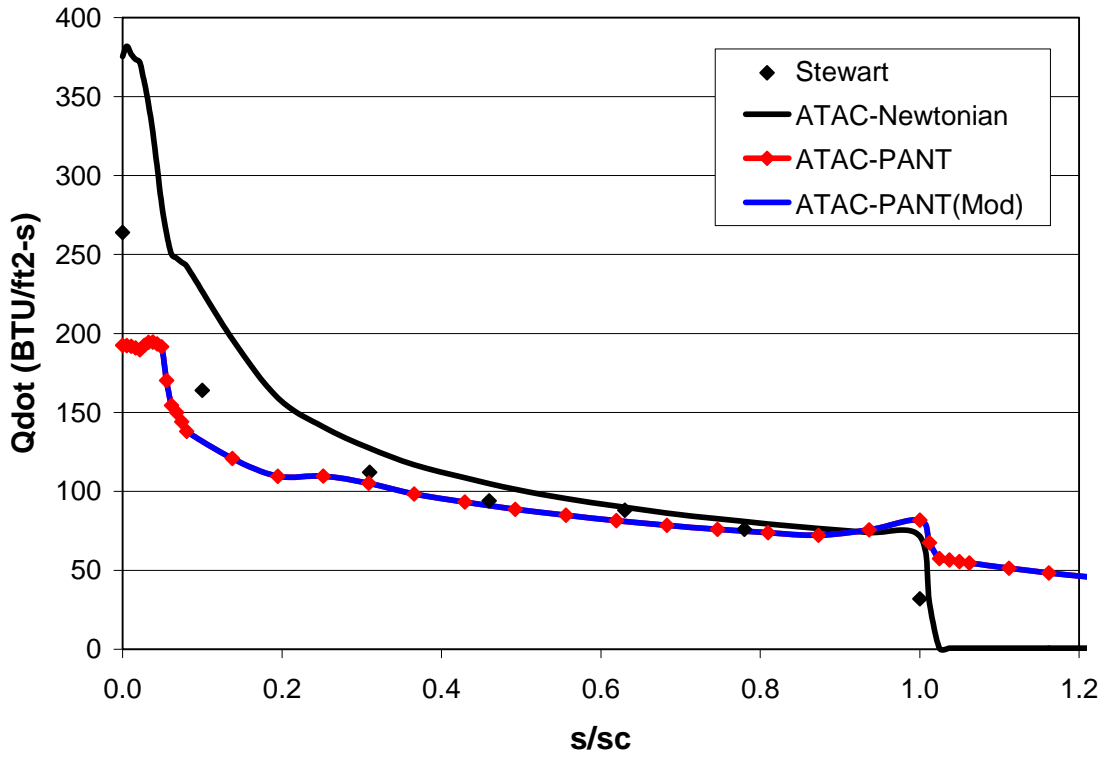
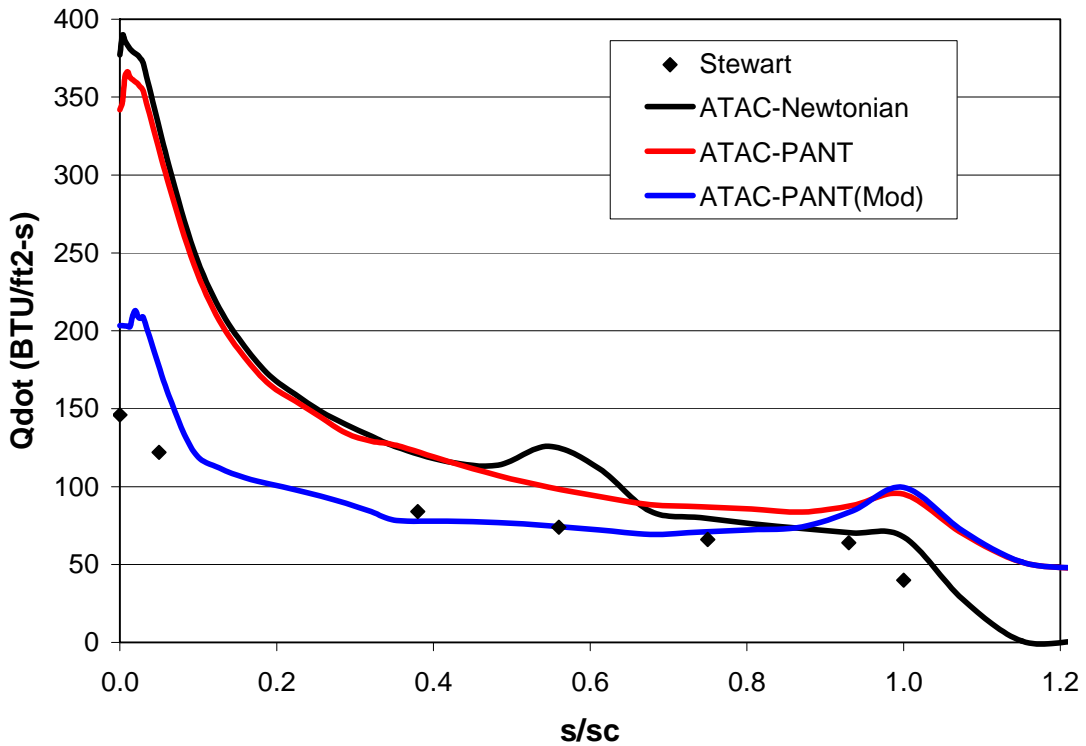**Figure 7: Comparison with Stewart's data for 50-deg conical section**

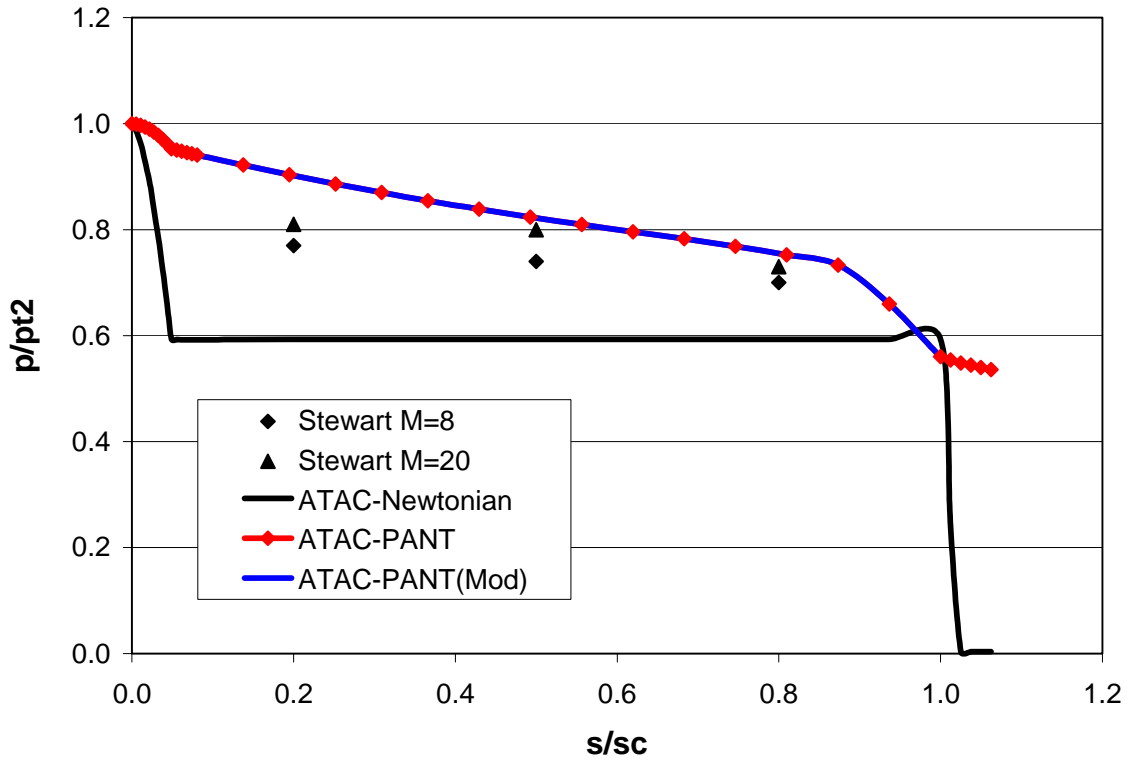**Figure 8: Comparison with Stewart's data for 70-deg conical section**

14

Figure 9: Comparison with Stewart's data for 52-deg conical section
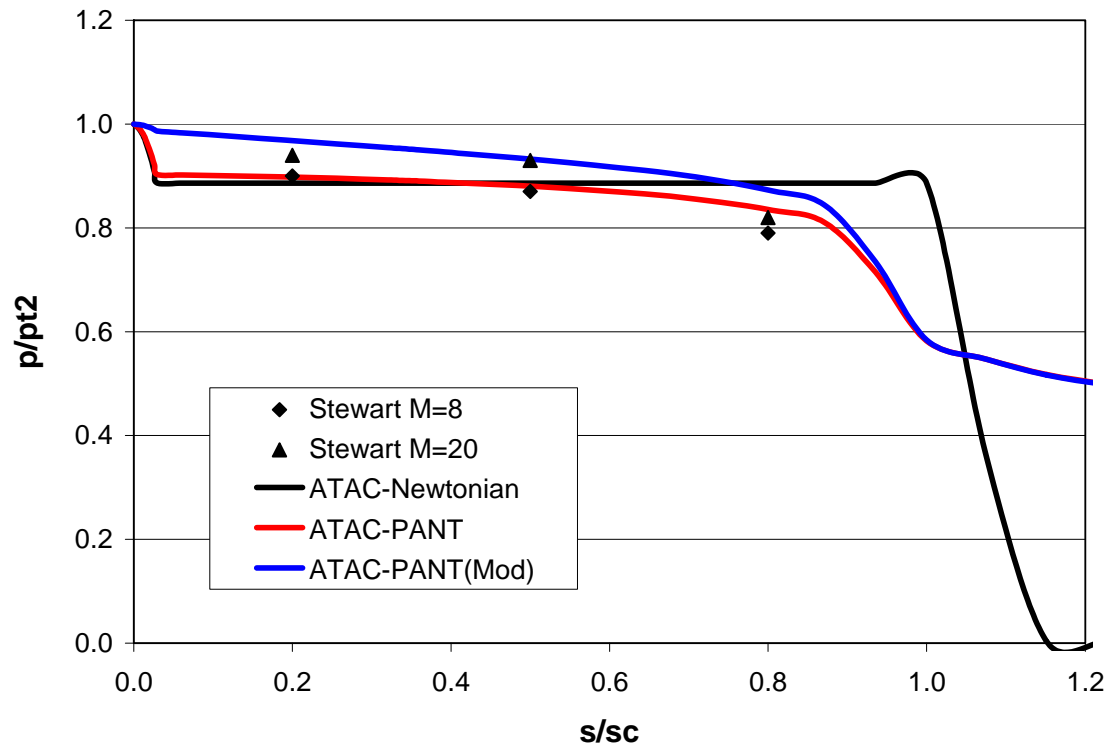

Figure 10: Comparison with Stewart's data for 70-deg conical section

point and the stagnation point heat flux. The results of these modifications are also shown in Figures 7 through 10. The pressures and heat flux for the 50 degree cone are the same with the modified nosetip logic since the R_n values did not change. For the 70 degree cone, the pressure on the conical section was in better agreement with the data (Figure 10) and the heat flux at the stagnation point was significantly lower (Figure 8).

The calculations for the MSL were redone using the modified nosetip logic to calculate the effective nose radius and the results are shown in Figure 11. There was a substantial improvement in the prediction of the stagnation point heat flux and the agreement with the data and LAURA predictions was much better. There is still a problem near the stagnation point where the MEIT procedure uses a linear pressure gradient model and we are continuing to examine the solution in this region.
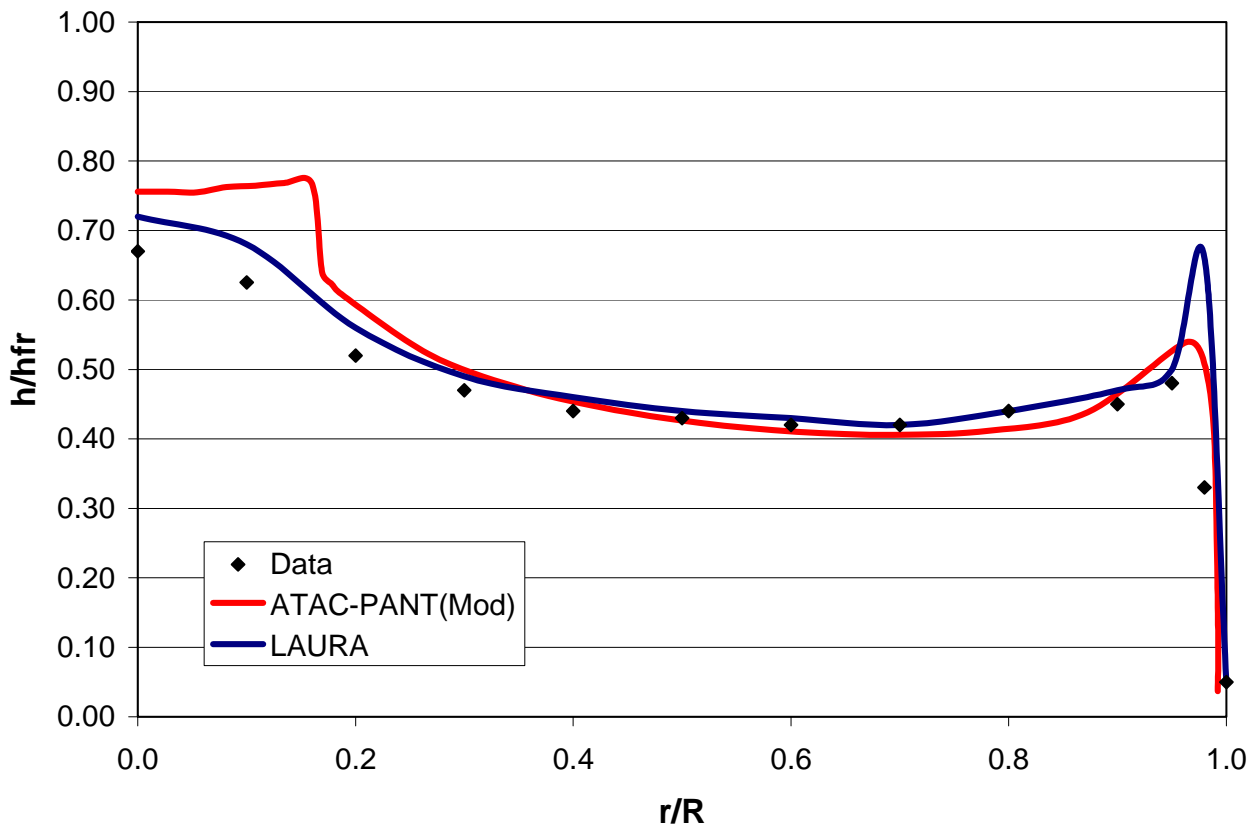
Figure 11: Comparison of modified R_n calculation with MSL data

SHUTTLE RE-ENTRY PREDICTIONS

The third test case presents calculations done for the Shuttle Orbiter and compares the predictions with thermocouple measurements from flight data. During the Infrared Sensing Aeroheating Flight Experiment (ISAFE),[21] Shuttle flights were selected to demonstrate the capability of ground-based infrared equipment and data reduction technique to measure the surface heating during flight. Shuttle aeroheating flight data are collected during each reentry using surface thermocouples and this large database could be used to validate the development of the IR sensing equipment.

Calculations were done for STS-96 and comparisons were made with thermocouples on the bottom surface. Reference 21 presents thermocouple data from the entry interface (400,000 ft) to landing (2000 seconds) for several thermocouples on the Orbiter. For our comparison, we selected four thermocouples located at various lengths down the centerline. The thermocouples were identified by the last three digits of the measurement system identification (MSID) nomenclature. The thermocouples and their locations are 468 (x/L=0.3), 597 (x/L=0.55), 590 (x/L=0.7) and 502 (x/L=0.95).

The Orbiter is a very complex configuration and required the use of the general patch option in ATAC. The surface patch model that was used in these calculations is shown in Figure 12. In general, model captures most of the features of the orbiter except for the body flap and the engine nozzles. Figure 13 presents the predicted surface temperatures at 1000 seconds after entry interface.

Figures 14 through 17 compare the ATAC predictions with the data from STS-96. In general, the predictions were in good agreement with the data. ATAC overpredicted the initial heating in the first 200 seconds and underpredicted the turbulent heating after 1300 seconds. For the first three thermocouples the maximum temperature during the laminar portion of the flight was well predicted. At the last station, ATAC underpredicted the maximum laminar temperature by 100 degrees. The angle of the body flap was not given in the paper but a small deflection could make a significant different in the heating on the flap.

Berry, Merski, and Blanchard[22] also present Shuttle heating data using the phosphor thermography technique. To test their data reduction and extrapolation method, they compared the extrapolated prediction with thermocouple data from STS-2. Figure 18 compares the ATAC prediction with the extrapolated phosphor thermography and with the STS-2 measurements. The agreement with the data is very good in the laminar region. ATAC is predicting the onset of transition earlier that the measurements indicate.

To demonstrate the efficiency of ATAC, the model for the STS-96 flight used 200 patches and 1864 CMA solutions. The calculation modeled 1900 seconds of flight time and performed 205 flowfield solutions with 52 streamlines each. The CPU time required for this calculation was 433 seconds on an 1.5 GHz Intel Pentium Processor.
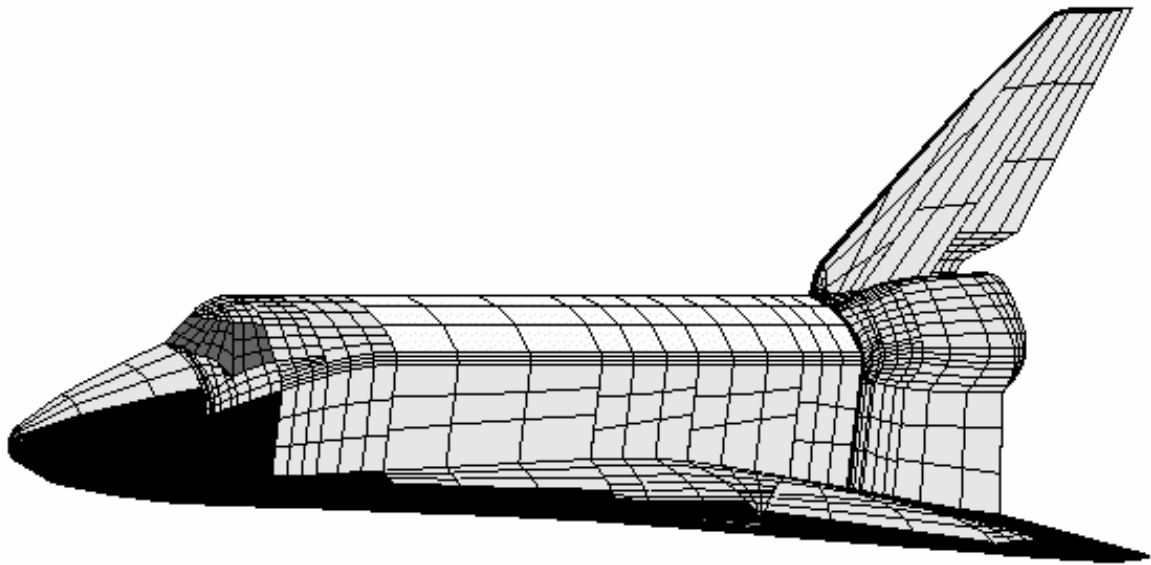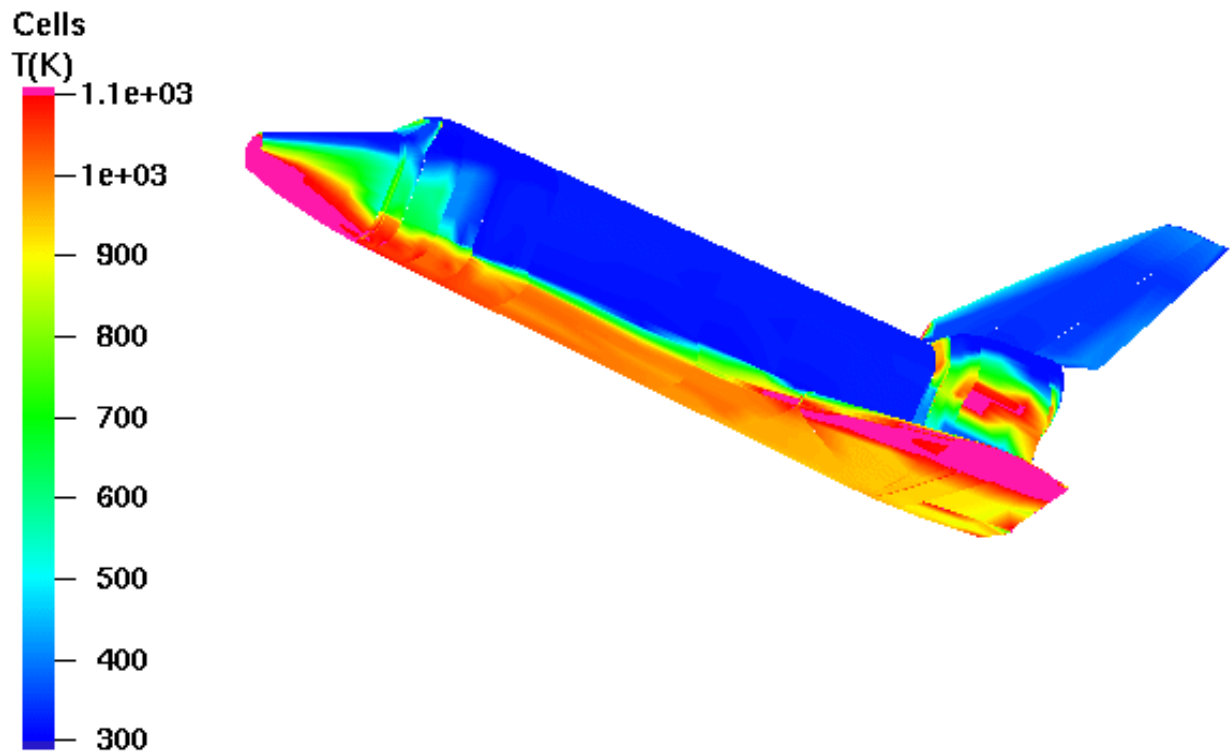
Figure 12: ATAC shuttle geometry

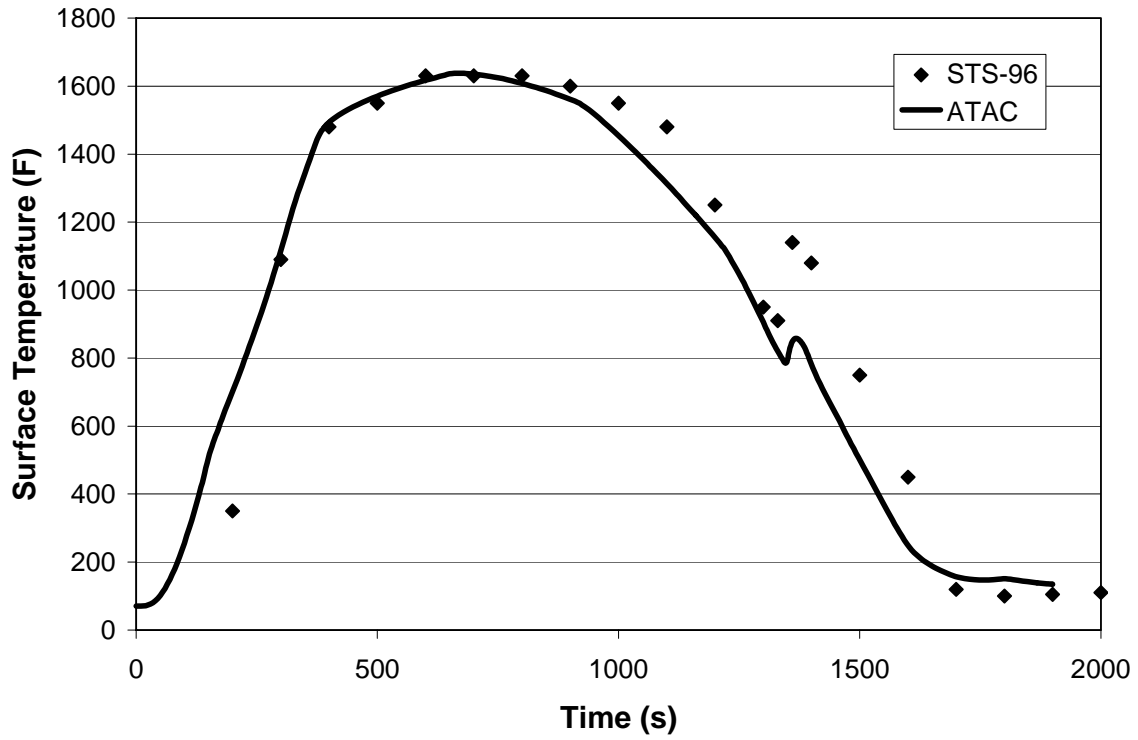**Figure 13: ATAC surface temperature contours at t=1000 s**

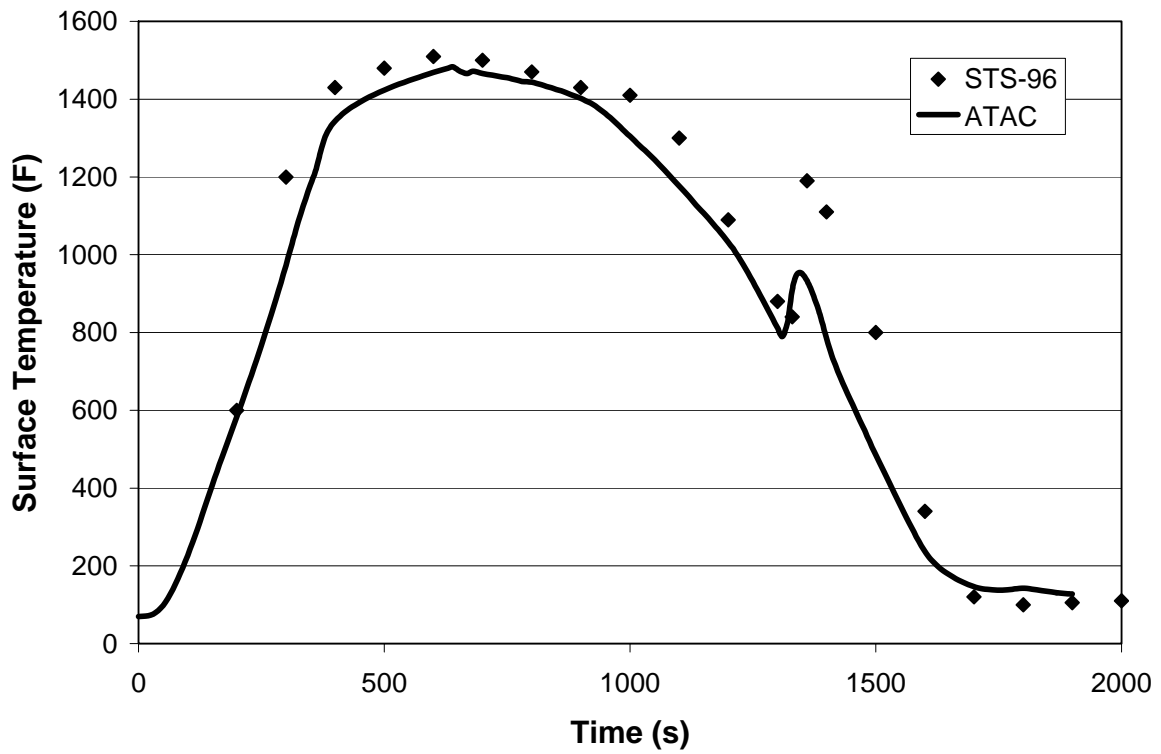**Figure 14: Comparison with thermocouple 468, x/L=0.30**

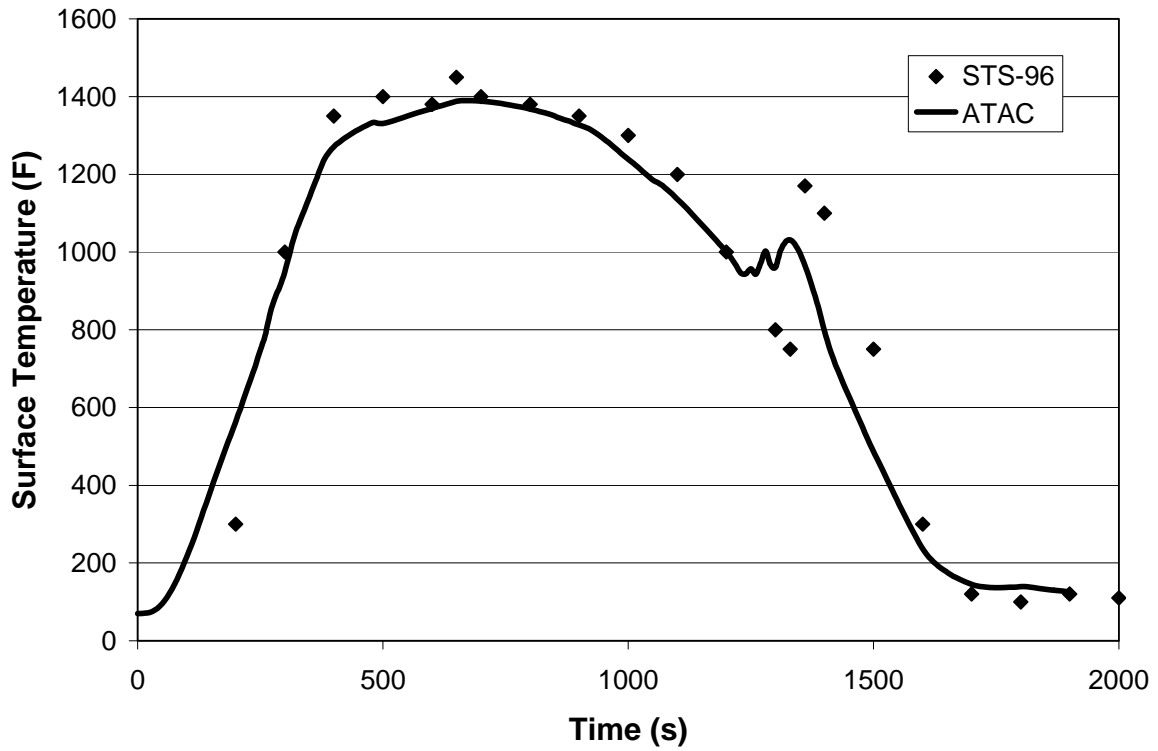**Figure 15: Comparison with thermocouple 597, x/L=0.55**

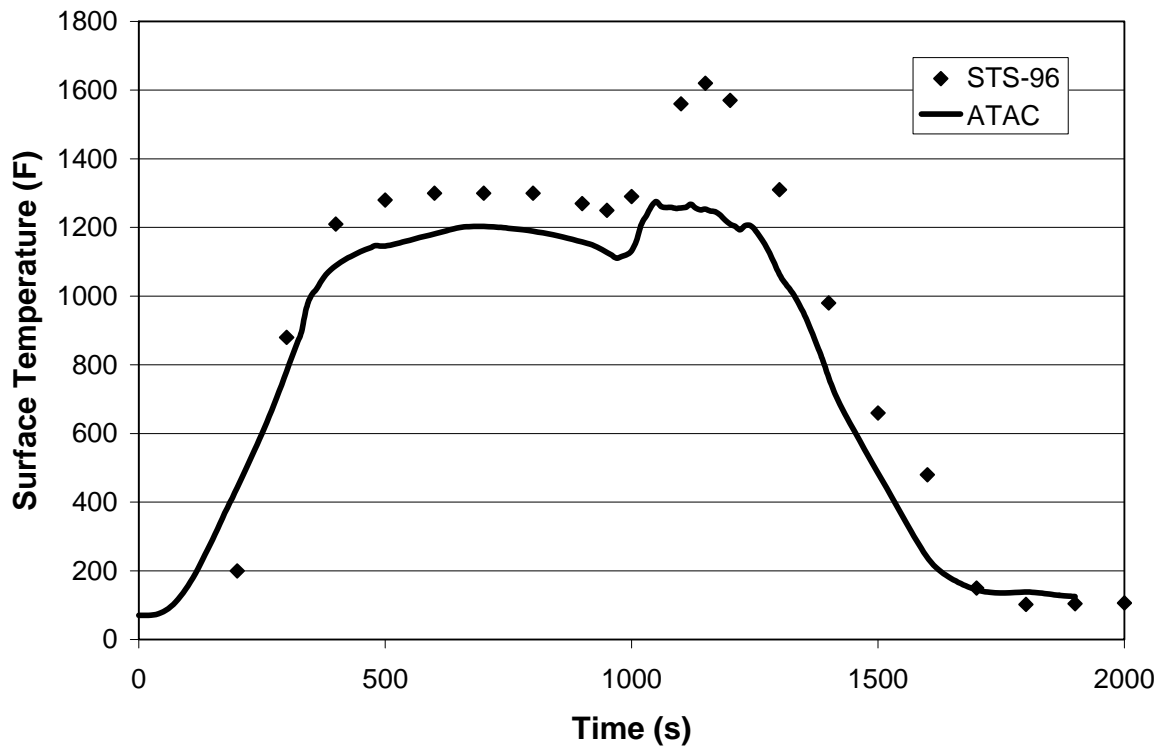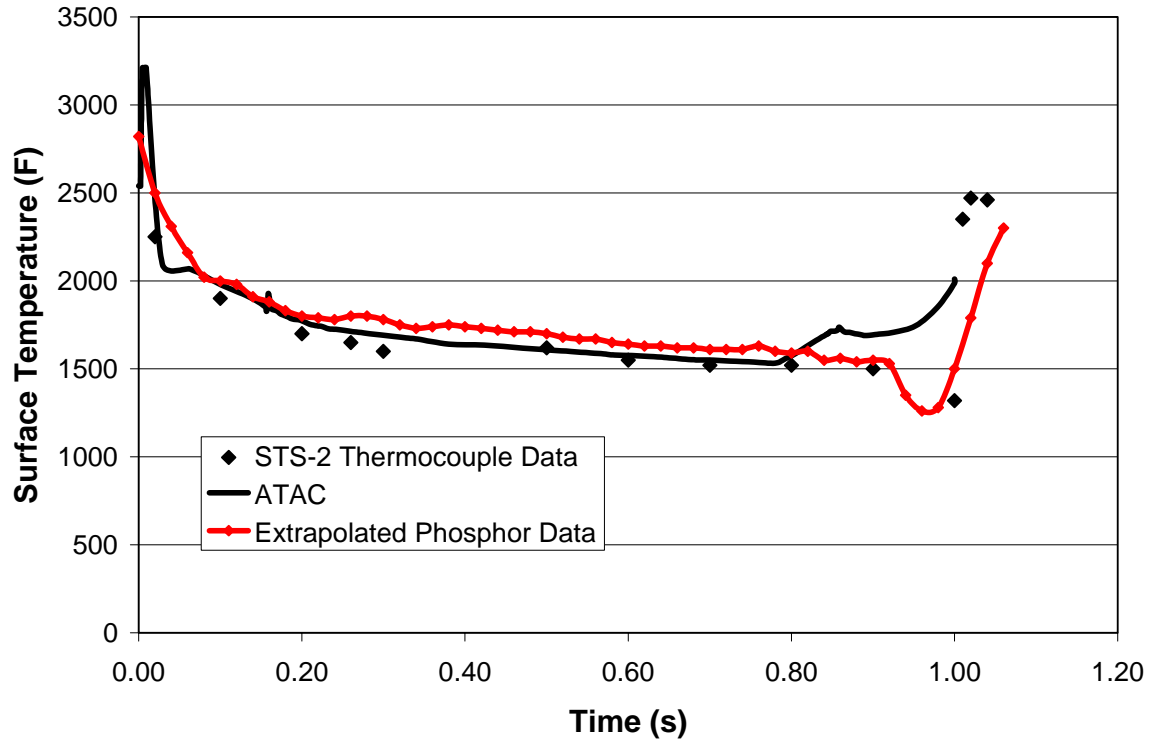**Figure 16: Comparison with thermocouple 590, x/L=0.7**

Figure 17: Comparison with thermocouple 502, x/L=0.95

Figure 18: Comparison with STS-2 thermocouple data at t=1130 s

CONCLUSIONS

The Aeroheating and Thermal Analysis Code (ATAC) has been demonstrated for both blunt body and space plane configurations. The code is capable of modeling complex configurations in a efficient manner and can provide good predictions for design and analysis. Comparisons with data from Viking Martian entries showed that the code was capable of providing good aerodynamic predictions from the continuum to the free-molecular flow regimes. Comparisons with the Mars Smart Lander showed that the nose radius calculation was limiting the ability of the PANT correlation to predict the velocity gradient at the stagnation point. Improvements in the procedures are needed to model the acceleration near the nosetip for the large-angle conical geometries. Comparison with Shuttle flight and wind tunnel data showed that the code gave good predictions along the centerline of the body even at 40 degrees angle attack.

REFERENCES

1. Murray, A. L., "User's Manual for the Maneuvering Aerotherm Shape Change Code (MASCC99)," Aerotherm Corporation, FR 6002-99-001, Huntsville, AL, Jan 1999.
2. "User's Manual: Aerotherm Charring Material Thermal Response and Ablation Program," Acurex Corporation, UM-87-11/ATD, Mt. View, CA, Aug, 1987.

3. Murray, A. L., "User's Manual for the Aeroheating and Thermal Analysis Code (ATAC3D)", ITT Aerotherm, FR 0608A-01-001, Huntsville, AL, Jan 2001.

4. Coons, S. A. and Herzog, B., "Surfaces for Computer-Aided Aircraft Design," AIAA Paper 67-895, 1967.

5. King, H. C., Muramoto, K. K., Murray, A. L., and Pronchick, S. W., "ABRES Shape Change Code (ASCC86): Technical Report and User's Manual," Acurex Corporation, FR-86-24/ATD, Mt View, CA, Dec 1986.

6. Andrews, J. S., "Steady State Airload Distribution on Hammerhead Shaped Payload of a Multistage Vehicle at Transonic Speeds," Boeing Company, D2-22947-1, Seattle, WA, Jan 1964.

7. Isaacson, L. K. and Jones, J. W., "Prediction Techniques for Pressures and Heat-Transfer Distributions Over Bodies of Revolution in High-Subsonic to Low-Supersonic Flight," Naval Weapons Center, NWC TP 4570, China Lake, CA, Nov 1968.

8. Timmer, H. G., "Ablation Aerodynamics for Slender Reentry Bodies," Air Force Flight Dynamics Laboratory, AFFDL-TR-70-27, Dayton, OH, Mar 1970.

9. Kutateladze, S. S. and Leont'ev, A. I., *Turbulent Boundary Layers in Compressible Gases*, Academic Press, 1964.

10. Kutateladze, S.S., "On the Turbulent Boundary Layer with Vanishing Viscosity," *Heat and Mass Transfer in Boundary Layer*, edited by N. Afgan, Z. Zaric, and P Anastasijevic, Volume 1, Proceedings of the International Summer School, Herceg Novi, Beograd, Sep 1968.

11. Schaaf, S. A. and Chambre, P. L., "Flow of Rarefied Gases," Section H pf Vol III, *Fundamentals of Gas Dynamics,* edited by H. W Emmons, Princeton Series, High Speed Aerodynamics and Jet Propulsion , Princeton University Press, Princeton, 1958..

12. Bird, G. A., *Molecular Gas Dynamics*. Clarendon Press, 1976.

13. Bird, G. A., "Monte-Carlo simulation in an engineering context," In S. S. Fisher, editor, *Progress in Astronautics and Aeronautics, Rarefied Gas Dynamics*, AIAA, 1981. Vol. 74, Pt. II.

14. Matting, F. W., "Approximate bridging relations in the transitional regime between continuum and free-molecular flows," *Journal of Spacecraft and Rockets, 8*(1):35-40, January 1971.

15. Wilmoth, R.G, Blanchard, R. C., and Moss, J. N., "Rarefied Transitional Bridging of Blunt Body Aerodynamics," 21st International Symposium of Rarefied Gas Dynamics, Marseille, France, July 26-31, 1998.

16. M. S. Ivanov, G. N. Markelov, S. F. Gimelshein, L.V. Mishina, A. N. Krylov, and N. V. Grechko, "High-Altitude Capsule Aerodynamics with Real Gas Effects," *Journal of Spacecraft and Rockets,* 35(1):16-22, 1986.

17. Hollis, B. R. and Liecthy, D. S., "Boundary Layer Transition Correlations and Aeroheating Predictions for Mars Smart Lander,", AIAA 2002-2745, 32nd AIAA Fluid Dynamics Conference and Exhibit, St, Louis, MO, June 24-26, 2002.

18. Murray, A. L., "Coupled Aeroheating/Ablation Analysis for Re-entry Vehicles," 14th Annual Thermal and Fluids Analysis Workshop, Hampton, VA, August 18-22, 2003.

19. Stewart, D. A. and Marvin, J. G., "Convection Heat-Transfer Rates on Large-Angle Conical Bodies at Hypersonic Speeds," NASA TN D-5526, November, 1969.

20. Stewart, D. A., and Inouye, M., "Shock Shapes and Pressure Distributions for Large-Angle Pointed Cones in Helium at Mach Numbers of 8 and 20," NASA TN D-5343, 1969.

21. Blanchard, R. C., Wilmoth, R. G., Glass, C. E., Merski, N. R., Berry, S. A., and Bozung, T. J., "Infrared Sensing Aeroheating Flight Experiment: STS-96 Flight Results," AIAA 2001-0352, 39th AIAA Aerospace Sciences Meeting and Exhibit, Reno, NV, January 8-11, 2001.
22. Berry, S. A., Merski, N. R., and Blanchard, R. C., "Wind Tunnel Measurements of Shuttle Orbiter Global Heating with Comparisons to Flight," AIAA 2002-4701, AIAA Atmospheric Flight Mechanics Conference, Monterey, CA, August 5-9, 2002.

NOMENCLATURE, ACRONYMS, ABBREVIATIONS

A	reference area, m^2
$C_f/2$	friction factor, $\tau_w / \rho_e u_e^2$
C_h	Stanton number
c_a	axial force coefficient
c_n	normal force coefficient
c_p	pressure coefficient
F	entrainment shape factor, $(\delta - \delta_e^*)/\Theta$
h	enthalpy, J/kg
h_r	recovery enthalpy, J/kg
h_t	total enthalpy $\equiv h + u^2/2$, J/kg
h_w	wall enthalpy, J/kg
H	shape factor, δ^*/Θ
$I_{x,y,z}$	influence coefficient
Kn	Knudsen number
$\hat{n}$	surface normal unit vector
p	pressure, N/m^2
Pr	Prandtl number
$\dot{q}$	wall heat flux, W/m^2
r	radial coordinate, m
Re	Reynolds number
R	recovery factor; gas constant, J/kg-K; streamtube radius, m
s	stream length measured from the stagnation point, m; molecular speed ratio for free molecular flow
t	unit surface tangent vector
T	temperature, K
u	boundary layer flow velocity tangent to surface, m/s; circumferential surface parameter
v	boundary layer flow velocity normal to surface, m/s
$\vec{v}$	tangential velocity vector, m/s
$\vec{V}_\infty$	freestream velocity vector, m/s
w	axial surface parameter
y	coordinate normal to the body surface

$\bar{y}$ shock radial location through which boundary layer edge streamline passes, m

α angle of attack, degrees; thermal accommodation coefficient

δ boundary layer thickness, m

δ^* boundary layer displacement thickness $\equiv \int_0^\delta 1-\left(\dfrac{\rho u}{\rho_e u_e}\right)dy$, m

θ body slope, degrees

Θ boundary layer momentum thickness, m

λ molecular mean free path, m

μ viscosity, kg/m-s

ρ density, kg/m^3

Φ energy thickness $\equiv \int_0^\delta \dfrac{\rho u}{\rho_e u_e}\left(\dfrac{h_{t,i}-h_t}{h_{t,e}-h_w}\right)dy$, m

σ tangential surface reflection coefficient

σ' normal surface reflection coefficient

Subscripts

e   boundary layer edge

ℓ laminar flow

t   turbulent flow

w   wall